Pergamon

Acta mater. 48 (2000) 4021–4033

Acta MATERIALIA

www.elsevier.com/locate/actamat

COMPOSITIONALLY GRADED MATERIALS WITH CRACKS NORMAL TO THE ELASTIC GRADIENT

C. -E. ROUSSEAU and H. V. TIPPUR†

Department of Mechanical Engineering, 202 Ross Hall, Auburn University, Auburn, AL 36849, USA

(Received 22 February 2000; received in revised form 26 June 2000; accepted 26 June 2000)

Abstract—Mixed-mode crack tip deformations and fracture parameters in glass-filled epoxy beams with cracks normal to the elastic gradient are studied. Crack tip fields are optically measured for different crack locations in the elastic gradient when subjected to symmetric pure bending. A companion finite element model is developed and validated by the measurements. The numerical model is then used to examine the influence of the elastic gradient on crack location by evaluating stress intensity factor, mode-mixity and energy release rate. For certain crack locations, computed stress intensity factors and energy release rates in the graded material exceed that of the bimaterial counterpart. However, when reconciled with measured critical values of the fracture parameters, graded beams show consistently better performance for all crack locations in the graded region. Crack kinking due to compositional gradients are examined and are successfully compared with the vanishing K_{II} criterion based on a locally homogeneous material behavior. © *2000 Acta Metallurgica Inc. Published by Elsevier Science Ltd. All rights reserved.*

Keywords: Functionally graded materials; Crack tip fields; Fracture toughness

1. INTRODUCTION

Compositionally or Functionally Graded Materials (FGMs) are those whose composition and hence the properties vary gradually as a function of position. This gradation may occur naturally or may be a byproduct of manufacturing processes. For example, bonding procedures such as cladding [1] or welding of dissimilar materials create an interfacial region, where transition from one material to the other takes place. Homogeneous materials may also acquire property gradation during service. For instance, a homogeneous material with one surface constantly exposed to environmental factors (say, nuclear radiation) from which another surface is insulated may experience embrittlement of the former with respect to the other [2]. Particles may also be mixed to various degrees into a matrix, forming a particulate composite with continuously changing properties [3]. For example, metal–ceramic composites with compositional gradients could offer excellent thermo-mechanical properties while reducing concerns about interfacial disbonding typical of discretely coated ceramic layers on a metal substrate.

Of interest to the present work is the fracture behavior of FGMs with cracks perpendicular to the elastic gradient. A review of some of the works completed in this area is as follows. Bao and Cai [4] have studied the delamination cracking and buckling of an FGM strip bonded to a homogeneous substrate. They have determined that in the presence of a crack perpendicular to the gradient and parallel to the interface, the fracture driving force and potential buckling are reduced in FGMs when compared to dissimilar bonded materials. Gu and Asaro [5] have performed theoretical studies for FGM cracks of the same configuration, including those having orthotropic material properties. They have also analyzed kinking of the crack for the isotropic case [6]. Erdogan *et al*. [7] have examined the crack tip singularity and determined it to be identical to that of a homogeneous material, regardless of the location of the crack. The same conclusions were reached by Jin and Noda [8]. Also of interest are numerical observations by Tohgo *et al*. [9], who have reported a decreasing size of the singular field with an increasing material property gradient. Sekine and Afsar [10] have developed an eigenstrain superposition method yielding the fracture toughness of an FGM from knowledge of its composition profile. Marur and Tippur [11] have numerically studied the influence of the gradient on the fracture parameters of FGMs sandwiched between two homogeneous strips having moduli equal to the ter-

† To whom all correspondence should be addressed. Fax: + 1-334-844-3307.

E-mail address: htippur@eng.auburn.edu (H.V. Tippur)

PII: S1359-6454(00)00202-0

minal moduli of the FGM. They varied the width of the FGM "insert" from one having a smaller slope so as to be equivalent to a homogeneous beam, and decreased it to a limit wherein the beam behaves as a bimaterial.

Experimental evaluation of cracked FGMs with cracks oriented normal to the elastic gradient are limited. Feasibility of full-filed optical measurement of mixed-mode crack tip deformation in compositionally graded medium was demonstrated in Butcher *et al*. [12]. The situation of a crack located at a sharp interface between a graded material and a homogeneous material was considered in that work as an example. Marur and Tippur [11] have demonstrated the possibility of measuring mixed-mode SIFs by optimally locating strain gages near an FGM crack.

Research presented in the current work addresses the influence of crack location along the graded region when subjected to configurationally symmetrical loading. Fracture parameters of FGMs are examined relative to bimaterial and homogeneous material counterparts experimentally and numerically. Fracture parameters are reconciled with actual crack initiation toughness measurements to assess FGM failure performance for various crack locations. The next section looks at the fabrication and characterization of the FGMs used in this study, then details fracture toughness tests performed on homogeneous materials, constituents of the FGMs. Next, Sections 3 and 4 describe the optical experiments and extraction of the stress intensity factors. Section 5 gives the details of the extensive finite element work. Finally, the results are discussed in Section 6.

2. MATERIAL PREPARATION AND CHARACTERIZATION

2.1. Preparation

The FGM used in this study was made of solid A-glass spheres of mean diameter 42 μm (28–75 μm range, with 50% finer than 42 μm) dispersed within a slow curing epoxy matrix. The latter is composed of 73.5 parts of pure epoxy and 26.5 parts of hardener, based on weight. The volume fraction of the spheres in the matrix varies gradually from 0 to 0.52 which results in a smooth and continuous variation in the material properties of the composite. The method of preparation of the FGM from these two constituents was first devised by Butcher *et al*. [12]. The material is cast in vertical molds (Fig. 1(a)) where the heavier glass spheres ($\rho = 2470$ kg/m^3) sink to the bottom, whereas the lighter epoxy ($\rho = 1150$ kg/m^3) floats to the top. The opposite motion of these two constituents creates a continuous compositional gradient. Concurrently, gelation of the matrix forestalls complete separation of the two. The mixture is allowed to cure for 18 h, at which point its elastic properties can be measured.

2.2. Elastic properties

Ultrasonic pulse-echo measurements were carried out at various locations along the gradient to obtain the local values of longitudinal velocity, C_l. A "C_l vs E" (where E is Young's modulus) look-up chart developed by Butcher *et al*. [12] for this specific glass/epoxy mixture was then used to retrieve the variation in elastic modulus within the FGM plate.

The casting process produced remarkably repeatable FGM gradients as shown in Fig. 1(b). The figure shows the Young's modulus variation of several of the cast plates. All castings exhibit an asymmetric sigmoidal behavior in elastic modulus. The region of varying properties exists between two regions consisting on the compliant side of pure epoxy, and on the stiff side of a glass/epoxy composite with a high concentration of glass spheres. These outlying materials are represented by the dashed horizontal lines on either sides of the symbols in Fig. 1(b). The ratio of the elastic moduli between the extreme ends of the gradient is 3:1, with a maximum of approximately 9 GPa at the glass-rich end.

A local non-dimensional variable ξ is introduced as shown in Fig. 1(b) and is set to zero at the transition between the compliant material and the beginning of the gradient. It is set to 1 at the transition where the glass beads reach saturation in the matrix. Thus the elastic gradient region ($0 < \xi < 1$) is defined within a span of about 37 mm. Note also the values of $\xi = 0.17$, 0.33, 0.58, and 0.83 indicated in the figure. At these locations, cracks were subsequently inserted for experimental evaluations.

In Fig. 2, Young's modulus and Poisson's ratio of *homogeneous* glass/epoxy composites are plotted with respect to volume fraction, V_f. The elastic modulus increases monotonically with V_f, whereas the Poisson's ratio decreases with V_f. The increase in elastic modulus is accounted for by the high modulus of the inclusions (69 GPa), resulting in a stiffer material. Conversely, the glass spheres lower the values of the Poisson's ratio, ν, as V_f increases.

Also included in Fig. 2 are curves representing variation of elastic modulus with respect to volume fraction as predicted by the Mori–Tanaka estimation for two phase mixtures [13], and the Halpin–Tsai lower bound estimation based on the "rule-of-mixtures". For the former, the bulk modulus κ and the shear modulus μ of the composite are given by:

$$\kappa = \kappa_m \left[1 + \frac{V_f}{\dfrac{3(1 - V_f)\kappa_m}{3\kappa_m + 4\mu_m} + \dfrac{\kappa_m}{\kappa_i - \kappa_m}} \right] \tag{1}$$

$$\mu = \mu_m \left[1 + \frac{V_f}{\dfrac{6(1 - V_f)(\kappa_m + 2\mu_m)}{5\,(3\kappa_m + 4\mu_m)} + \dfrac{\mu_m}{\mu_i - \mu_m}} \right] \tag{2}$$

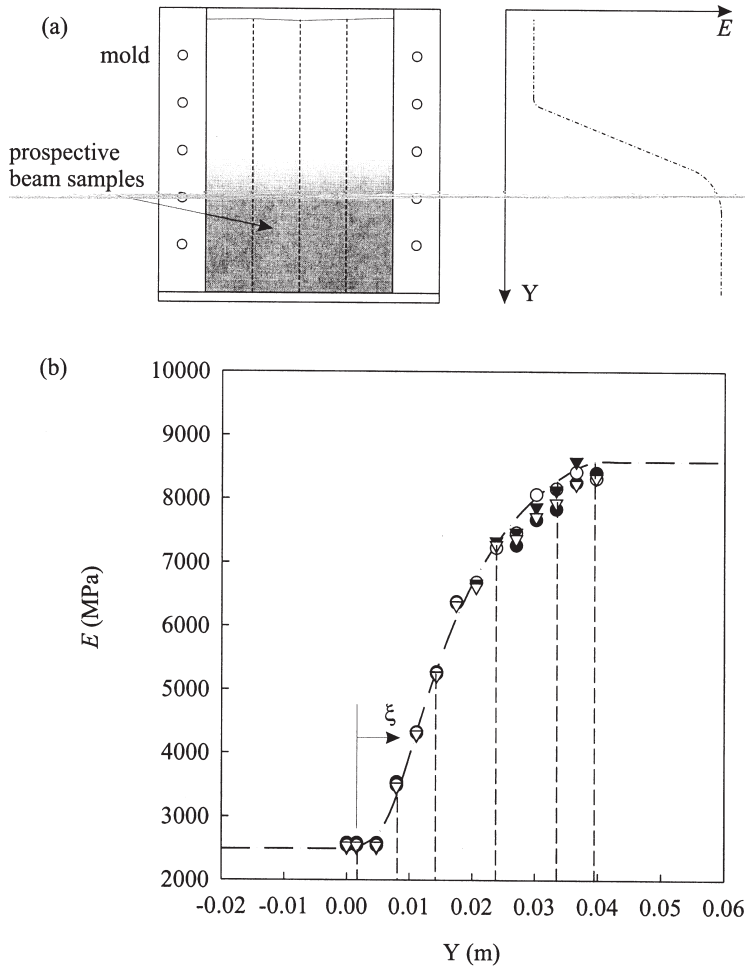

Fig. 1. Young's modulus variation in FGM plates (each symbol corresponds to a different casting). Vertical lines correspond respectively to $\xi = 0$, 0.17, 0.33, 0.58, 0.83 and 1.

where the subscripts m and i denote the matrix and the inclusions, respectively. The Young's modulus of the composite is obtained from the above two moduli by simultaneously solving $\kappa = E/3(1 - 2\nu)$ and $\mu = E/2(1 + \nu)$. The Halpin–Tsai prediction for the elastic modulus of the composite is:

$$E = \frac{E_m(E_i - 2sE_m + 2sV_fE_i - 2sV_fE_m)}{E_i - 2sE_m - V_fE_i + V_fE_m} \quad (3)$$

where s, the aspect ratio, is 1 for spherical inclusions. Values of $E_m = 3$ GPa, $E_i = 69$ GPa, $\nu_m = 0.35$, and $\nu_i = 0.15$ were used for evaluating E and ν of the composite. Evidently, the Mori–Tanaka prediction follows the experimental measurements closely. On the other hand, the Halpin–Tsai equation consistently over-predicts the elastic modulus.

In addition to FGMs, homogeneous and bimaterial plates were also cast, for comparison with the former. Two homogeneous plates with volume fractions of glass beads in the epoxy matrix of zero and 0.52, respectively, were prepared for experimental investigation. Also, bimaterial samples with the two sides having volume fractions of zero and 0.52, respectively, were fabricated. Note that these two values of V_f correspond to the volume fractions of the compliant and stiff sides of the FGM, respectively.

2.3. Crack initiation toughness

Evaluation of the fracture toughness of the glass/epoxy composite was undertaken by imposing quasi-static loads upon homogeneous specimens with edge cracks. These homogeneous beams with volume fractions varying from 0.0 to 0.5 had dimensions of 100 mm × 20 mm × 6 mm and were loaded in a three-point bending configuration at a cross-head speed to 0.025 mm/min.* A method was devised to create

* A few crack initiation toughness data for the material were previously reported by Butcher *et al*. [12] for the lower and upper bounds of volume fraction of glass beads in the

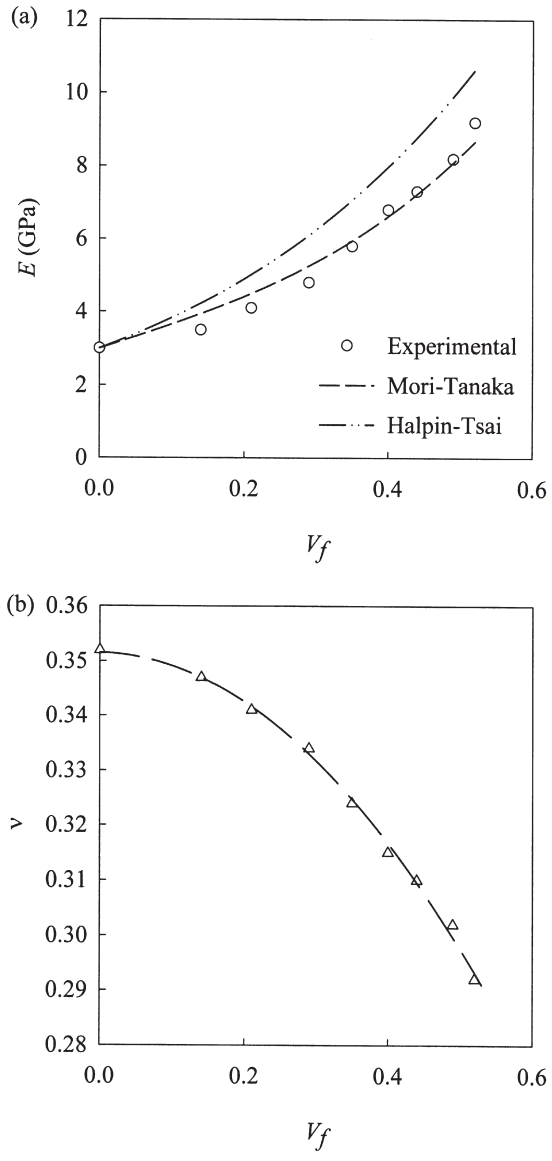

Fig. 2. Variation of static (a) Young's modulus and (b) Poisson's ratio with volume fraction of glass spheres in epoxy matrix.

sharp cracks in these samples. Edge notches (~ 150 μm wide) were cut into them, after which wedges were introduced into the notches. Application of a controlled force to the wedges extended the notches a few millimeters into natural, sharp cracks.

In addition to the above, fracture tests were also conducted on bimaterial specimens. The latter were fabricated by casting a half plate of homogeneous material with volume fraction of 0.52 and allowing it to cure fully. Then, uncured epoxy was poured into the mold and allowed to cure, to form a bimaterial. Beam samples of 100 mm × 20 mm × 6 mm were machined from these plates. As with the homogeneous specimens, an edge notch was cut at the interface and allowed to extend into a sharp crack.

A minimum of five samples were included in the bimaterial group and in each of the homogeneous groups with different volume fraction of glass. In all, over 100 tests were carried out. Each pre-cracked beam was subjected to a slow and controlled loading rate by an Instron-4465 Universal Testing Machine. For all the specimens, the variation of load with cross-head displacement was linear. Upon reaching the breaking load, P_{cr}, a sudden load drop was observed, with the material experiencing unstable fracture. The breaking load was used for calculating the crack initiation (critical) fracture parameters.

A summary of the test results is shown in Fig. 3. Fig. 3(a) shows the variation of critical values of stress intensity factor, K_{cr}, with respect to volume fraction. At low volume fractions, K_{cr} increases rapidly with increasing volume fraction. Moloney *et al.* [14] have likewise observed increases in toughness of particulate-filled epoxide resins at low volume fraction. At higher volume fractions, beyond $V_f \sim 0.25$, K_{cr} levels off, and even seems to show a slight decreasing trend. Behavior of the composite is different when material stiffness is taken into account. Accordingly, critical values of energy release rates, increase rapidly up to $V_f \sim 0.25$, then decrease at a slower rate (Fig. 3(b)).

For comparative purposes, critical values of SIF, $(\mathbf{K}_b)_{cr}$, and energy release rate, $(G_b)_{cr}$, for bimaterials were also determined. At crack initiation [15],

$$(G_b)_{cr} = \frac{1}{E^* \cosh^2(\pi\varepsilon)} |(K_b)_{cr}|^2 \tag{4}$$

where $\frac{1}{E^*} = \frac{1}{2}\left(\frac{1}{E_1} + \frac{1}{E_2}\right)$ and E_1 and E_2 are Young's moduli of the bimaterial. It should be noted that $(G_b)_{cr}$ for bimaterials is a function of crack tip mode-mixity ψ_b [16,17] defined as the phase of the complex SIF $(\mathbf{K}a^{i\varepsilon})$. The measured value of $(G_b)_{cr}$ is ~ 0.3 N/mm at a mode mixity of 4.4°.

Figures 3(c) and (d) show the scanning electron micrographs of fracture surfaces from the above tests at two different volume fractions. These micrographs do not show evidence of fractured filler material while "footprints" of debonded particles or intact particles in the epoxy matrix cavity are abundant. So, it can be concluded that the crack has made its way along the interfaces between the two constituents of the composite, thus avoiding the inclusions. Thereby, a tortuous crack path is created resulting in the formation of a greater surface area and an increase in the resistance to crack growth. The micrograph of a fractured surface from a specimen having a higher glass concentration, Fig. 3(d), illustrates potential reasons

epoxy matrix. However, that data corresponds to failure of discretely bonded strip. Further, thin Teflon tape inserts served as cracks.

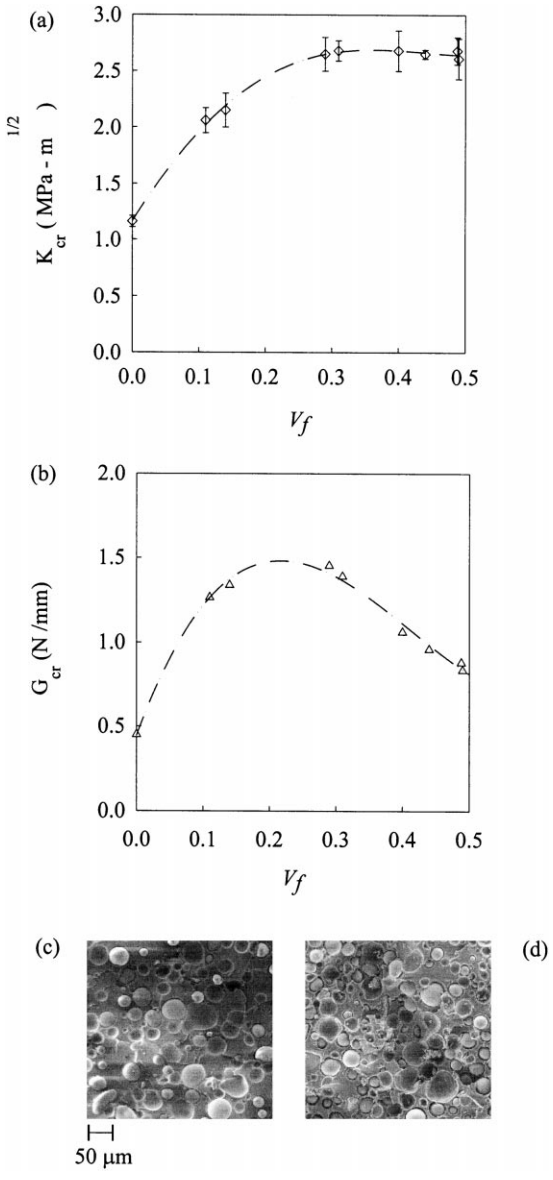

Fig. 3. Variation of critical stress intensity factor (a), crack initiation toughness (b), with volume fraction of homogeneous glass-filled epoxy composite. Fractured surface (c) $V_f = 0.16$, (d) $V_f = 0.30$.

for the apparent leveling in toughness values. Because of the high glass concentration, the possibility of having unwetted (filler particle clusters touching each other) neighboring glass spheres acting as microdefects increases and weakens the material. Therefore, the overall fracture toughness becomes essentially a competition between enhancement due to crack front twisting and turning and reduction from microdefect coalescence.

3. EXPERIMENTS

3.1. Specimen

The FGM beam specimens were made from large cast sheets having a variation in Young's modulus as shown in Fig. 1(a). In these, a 37 mm long elastic gradient is saddled by pure epoxy at one end and by a composite with high concentration of glass beads ($V_f = 0.5$) at the other end. From each sheet, several samples were machined, with the following dimensions (see inset in Fig. 4): 120 mm (gradient direction) × 22 mm × 6 mm. Also, edge notches 6 mm deep, with a root radius of 150 μm, were cut into the samples, perpendicular to the material gradient. Examination of the crack tip region in the optical interferometer did not reveal any residual stresses subsequent to the insertion of the notch. Experiments were conducted with cracks at the following locations of ξ: 0.17, 0.33, 0.58 and 0.83. The relevant material properties at these crack locations are shown in Table 1. Homogeneous and bimaterial specimens having the same dimensions as the FGMs were also machined for comparative testing.

The composite materials used in this study are opaque, and thus a reflection interferometer was used during optical measurements. Therefore, the surfaces to be interrogated were machined flat. Then the aluminum coating on a borosilicate optical flat (surface accuracy: $\sim 4\lambda$/inch) was transferred unto the specimen surfaces to make them specular reflective.

3.2. Optical set-up and measurements

A schematic of the reflection Coherent Gradient Sensing (CGS) set-up is shown in Fig. 4. A collimated beam of laser light (approximately 50 mm in diameter, $\lambda = 633$ nm) was used to interrogate the specular surface of the specimen. In the optical set-up, the reflected beam (object wave front) is directed towards a pair of Ronchi gratings. The object wave front is then laterally sheared in the direction perpendicular to the grating lines as shown. A filtering lens is used to collect all the sheared wave fronts propagating in discrete directions and the spectral contents appear as a linear array of spots on the back focal plane of the lens. Of these spots, either the $+1$ or the -1 diffraction spot is filtered and imaged. The image consists of two laterally sheared light beams with interference fringes in the overlapping area. The information received by the camera represents contours of constant gradients of out-of-plane displacement w with respect to the x- or y-axis, depending on the orientation of the Ronchi gratings [18]. In the present work, the gratings lines are oriented perpendicular to the crack. Therefore, the governing equation describes the non-planarity of the sample surface as,

$$\frac{\partial w}{\partial x} = \frac{Np}{2\Delta},\ N = 0, \pm 1, \pm 2, \ldots, \tag{5}$$

where N denotes fringe orders, p is the pitch of the gratings (25 μm), and Δ is the grating separation distance (47 mm). For plane stress conditions, the out-

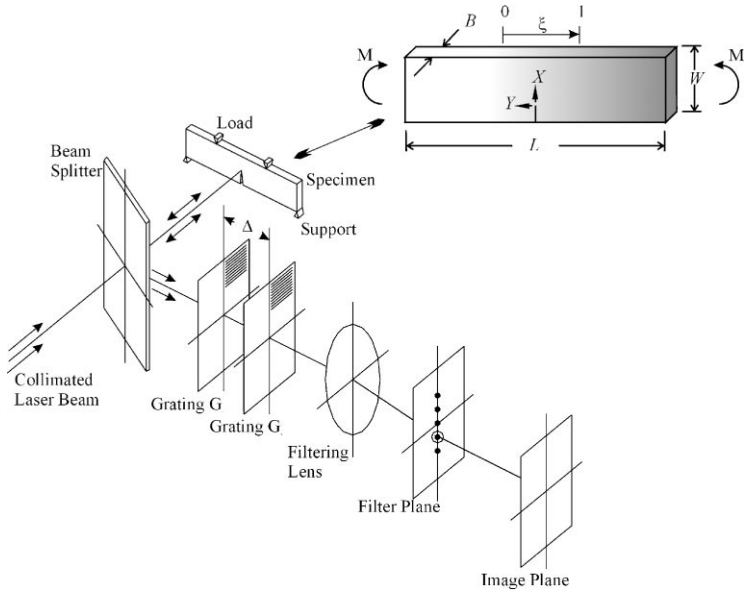

Fig. 4. Schematic of functionally graded beam and reflection CGS optical set-up used for mapping crack tip deformations.

Table 1. Material properties at various crack locations in the FGM

ξ	V_f	E (MPa)	ν	K_{Ic} (MPa $\sqrt{m}$)
0.0	0.0	3000	0.35	1.2
0.17	0.11	3300	0.34	2.1
0.33	0.31	5300	0.33	2.7
0.58	0.44	7300	0.31	2.7
0.83	0.49	8300	0.30	2.6
1.0	0.52	8600	0.29	2.6

of-plane displacement w can be related to the average strain in the thickness direction and in-plane stress components as, $\varepsilon_z \cong \frac{2w}{B} = \frac{-\nu}{E}(\sigma_x + \sigma_y)$, or,

$$w = -\frac{\nu B}{2}\left(\frac{\sigma_x + \sigma_y}{E}\right) \tag{6}$$

where B is the undeformed thickness of the sample.

The specimens were loaded in four-point bending, with a support span of 120 mm, and a constant moment over 60 mm in the mid-span. An Instron Universal Testing Machine provided displacement controlled loading at a cross-head speed of 0.25 mm/min. Examples of fringes representing gradients of out-of-plane deformations in the vicinity of the crack are shown in Figs 5(a) and (b) for the FGMs with cracks located at $\xi = 0.33$ and 0.58, respectively. The sensitivity of the optical measurements is 0.015°/fringe. Although the cracked beams are subjected to configurationally symmetric loading, note that the fringes display asymmetry about the crack plane due to the elastic gradient. However, note that the overall behavior is mode-I dominant, since fringes are only mildly asymmetric about the x-axis.

The fringe patterns of the FGMs are clearly in contrast with the ones for the bimaterial (Fig. 5(c)). The fringes from the stiff side are substantially smaller than those of the compliant side, behind the crack, and may not even be perceived ahead of it in the stiff region. Also presented are the fringes from the homogeneous sample (Fig. 5(d)) with high concentration of the filler. Note that the fringe patterns of the FGMs and the homogeneous specimens are similar, indicating mode-I dominant deformation in FGMs. Note that these interferograms in Fig. 5 were recorded at different load levels and hence, absolute sizes of the fringes cannot be compared directly.

4. EXPERIMENTAL EVALUATION OF SIFS

Consider a nonhomogeneous material with Young's modulus varying in an arbitrary direction. When E is continuous and piecewise differentiable, Jin and Noda [8] have shown that the Airy stress function is biharmonic, similar to the singular solution at the crack tip of a homogeneous material.

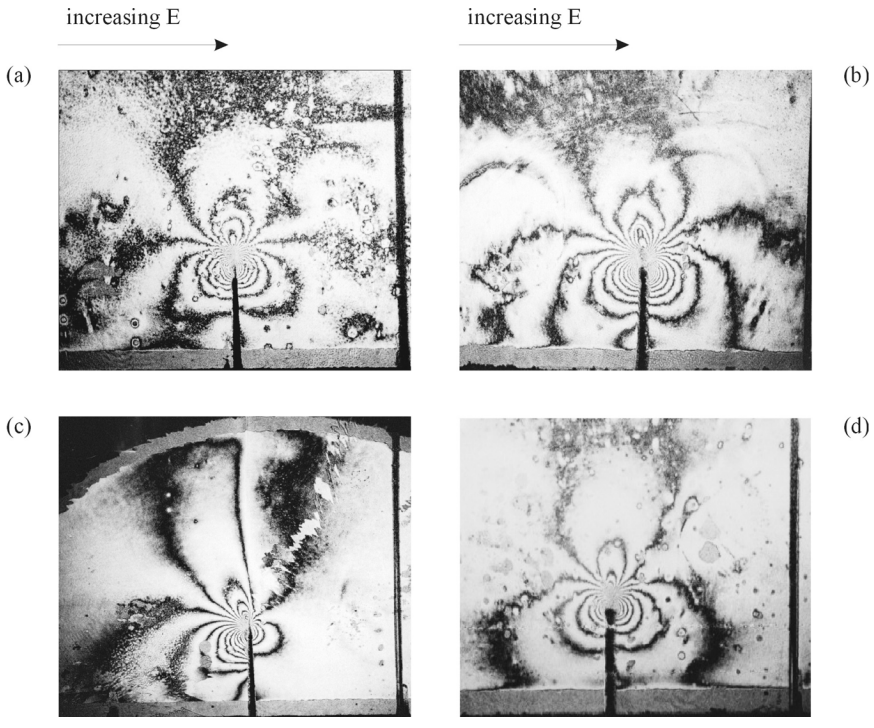

Fig. 5. Crack tip interference representing $\delta w/\delta x$ contours for FGMs with ξ equal to (a) 0.33, (b) 0.58, respectively, and $6M/BW^2$ equal to (a) 14.6 MPa, and (b) 14.1 MPa; (c) bimaterial ($V_f = 0.0$ and 0.5, $6M/BW^2 = 8.5$ MPa) and (d) homogeneous glass/epoxy composite ($V_f = 0.5$, $6M/BW^2 = 10.4$ MPa). Distance from crack plane to drawn line is approximately 10 mm.

They have concluded that regardless of the material gradient, singularity and angular stress gradient at the crack tip are identical to the equivalent conditions in a homogeneous material. As a result, assuming only in-plane deformations, the stresses at the crack tip of an FGM with continuous elastic gradient are:

$$\sigma_{ij}(r,\theta) \cong \frac{K_I}{\sqrt{2\pi r}} f_{ij}^{I}(\theta) + \frac{K_{II}}{\sqrt{2\pi r}} f_{ij}^{II}(\theta), \ (i,j = x,y) \qquad (7)$$

In the above, K_I and K_{II} are the mode-I and mode-II stress intensity factors, and the functions f_{ij}^{I} and f_{ij}^{II} are identical to the angular functions present in homogeneous definition of crack tip stresses. Variables r and θ are polar coordinates originating at the crack tip.

The stress field for a bimaterial crack differs from Eq. (7). The near tip fields show an oscillatory inverse $\sqrt{r}$ singularity and the angular functions are influenced by the elastic mismatch parameter $\varepsilon = \varepsilon(\mu_1,\mu_2,\kappa_1,\kappa_2)$ [19] as:

$$\sigma_{ij} \cong \frac{1}{\sqrt{2\pi r}} [K_1 \hat{f}_1(\theta;\ln r,\varepsilon) + K_2 \hat{f}_2(\theta;\ln r,\varepsilon)] \qquad (8)$$

where $\hat{f}_1$ and $\hat{f}_2$ are the appropriate angular functions.

With two in-plane modes of crack tip deformation being present, a complex stress intensity factor can be defined [11] for FGMs as: $\mathbf{K} = K_I + iK_{II}$, and bimaterials as $\mathbf{K} = K_1 + iK_2$. The phase angle of $\mathbf{K}$ is the mode-mixity ψ.

Explicit expressions relating CGS interferograms and the deformation field for FGM and bimaterials are, respectively:

$$\frac{-\nu B \delta}{E_0 \sqrt{2\pi} \delta x} \left[K_I r^{-1/2} \cos\frac{\theta}{2} - K_{II} r^{-1/2} \sin\frac{\theta}{2} \right] = \frac{Np}{2\Delta} \qquad (9)$$

$$\frac{-\nu B}{E_0 \sqrt{2\pi} \cosh(\pi\varepsilon)} \frac{\delta}{\delta x} \left\{ e^{\varepsilon(\theta-\pi)} r^{-1/2} \left[K_1 \cos\left\{ \frac{\theta}{2} + \varepsilon \ln\frac{r}{a} \right\} - K_2 \sin\left\{ \frac{\theta}{2} + \varepsilon \ln\frac{r}{a} \right\} \right] \right\} = \frac{Np}{2\Delta} \qquad (10)$$

where a difference interpretation of Eq. (5) is used, with $\delta(.)$ being the difference operator. The fringe patterns were digitized in the vicinity of the crack tip to obtain their polar coordinates and fringe orders. In doing so, some restrictions were placed on the data collection in order to effectively deal with crack tip triaxiality. In homogeneous materials, a region of predominantly three-dimensional stress is known to exist between the crack tip and a value of $r/B = 0.5$ [20]. Further, previous experiments [18, 21] have shown

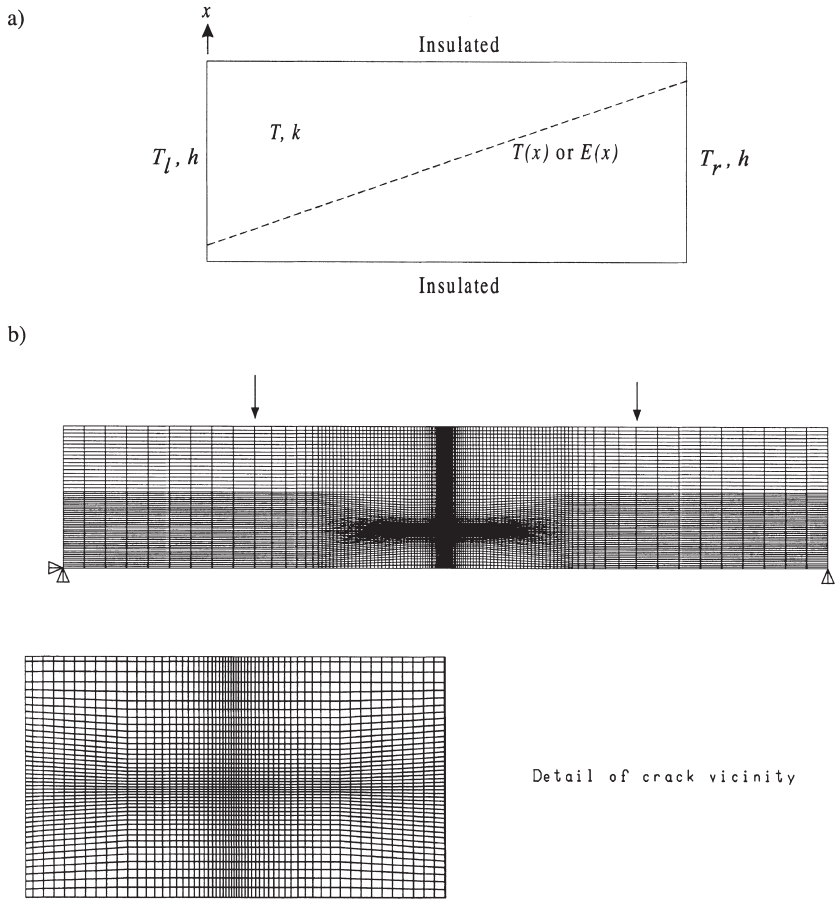

Fig. 6. Numerical model: (a) thermomechanical analysis to apply Young's modulus variation; (b) finite element discretization.

that triaxiality is minimal, behind the crack tip ($|\theta| > 90°$) under mode-I dominant conditions. Accordingly, only data from the region ($r/B > 0.5$, $90° < |\theta| < 135°$) was used in the analysis. An overdeterministic multi-parameter least-squares analysis of the data was conducted, and values of $\mathbf{K}$ and ψ were obtained. Comparison of results within FGMs, and between FGMs, and bimaterials are presented in Section 6.

5. NUMERICAL EVALUATION OF SIFS

Next, a finite element model was developed using the ANSYS™ software package. The model was subsequently used for capturing the influence of the elastic gradient on the fracture behavior and performance of FGMs relative to bimaterial and homogeneous material counterparts. The plane stress elasto-static finite element models with cracks located as in the experiments, consisted of about 10,000 eight-noded isoparametric elements with 30,000 nodes with two degrees of freedom per node. A typical model is shown in Fig. 6. No special crack tip elements were used in these models. The numerical models were subjected to four-point bending as in the experiments. Variations of Young's modulus and Poisson's ratio were then applied to the discretized domain. This is generally done by discretizing a rectangular domain into columns of elements and imposing a constant value of Young's modulus to each column of elements to realize stepwise change in the properties [12]. Alternatively,* a piecewise linear (or, higher order) variation would be more attractive and precise. Accordingly, a method of utilizing standard modules available in most finite element packages to implement a linear variation of Young's modulus within an element is accomplished as follows.

Consider a rectangular homogeneous isotropic continuum with an arbitrary uniform thermal conductivity k and a uniform initial temperature T. Let the

* Alternative methods of imposing elastic property gradients in FEA include special finite elements developed by Lee and Erdogan [22] and a user-defined subroutine for the ABAQUS software package developed by Giannakopoulos and Suresh [23].

horizontal edges be insulated as shown in Fig. 6. Assume further that the convective heat transfer coefficients for the left and right surfaces have the same arbitrary value, h. When this body is subjected to temperatures T_l and T_r at the left and right edges, respectively, upon reaching steady state, a linear temperature from T_l at the left edge to T_r at the right edge is realized. Discretizing the domain into finite elements and solving the governing equation for steady state heat flow will therefore result in linearly varying nodal temperatures with respect to position in the y-direction (along the length of the beam). (If needed, nonlinear temperature distributions could be implemented in several ways, for instance, by introducing heat generation rates at strategic locations of the finite element model.)

The nodal temperatures thus obtained can be used as thermal loading into a structural finite element model. However, temperature variations will induce undesirable (for the current work) thermal stresses. This can be remedied easily by setting the coefficient of thermal expansion α_o to zero, thus returning the material to its stress free condition. Simultaneously, by defining the material properties (in this case Young's modulus and Poisson's ratio for the FGM) as linear functions of temperature, results in the desired nodal material property variation which follows the temperature gradient accurately.

The numerical stress intensity factors were obtained by using regression analysis of the computed crack tip opening displacements. The displacement jumps across the crack faces of bimaterials are given by:

$$(\delta_y + i\delta_x)|_{\theta = \pm\pi, r\to 0} = \left(\frac{1}{E_1} + \frac{1}{E_2}\right)\frac{4|\bar{K}|e^{i\psi}\gamma^{i\varepsilon}}{(1 + 2i\varepsilon)\cosh(\pi\varepsilon)}\sqrt{\frac{r}{2\pi}} \tag{11}$$

E_1 and E_2 in the above denote Young's moduli of the two halves of the bimaterial. For homogeneous materials, after setting $\varepsilon = 0$, equation (11) reduces to the following, which is also valid for FGM in the limit $r\to 0$:

$$\delta_y + i\delta_x|_{\theta = \pm\pi, r\to 0} = \frac{8|\bar{K}|e^{i\psi}}{E_0}\sqrt{\frac{r}{2\pi}} \tag{12}$$

Here, E_o is the crack tip Young's modulus. The variation of $\bar{K}(r, \pm\pi)$ obtained from the finite element solution is plotted and its extrapolated value at the crack tip is:

$$|K| = \lim_{r\to 0}|\bar{K}| \tag{13}$$

For plane stress conditions the energy release rate G and stress intensity factors are related by $G_b = \left(\frac{1}{E_1} + \frac{1}{E_2}\right)\frac{K_1^2 + K_2^2}{2\cosh^2(\pi\varepsilon)}$, for bimaterials and $G = (K_I^2 + K_{II}^2)/E_o$ for homogeneous materials and FGMs as $r\to 0$.

6. RESULTS AND DISCUSSIONS

6.1. Experimental validation of the FE model

Companion finite element analyses of the experiments described in Section 4 were undertaken, from which stress intensity factors were extracted as outlined in Section 5. Both experimental and numerical results are compared in Table 2. The stress intensity factors are normalized by $\sigma_o\sqrt{(\pi a)}$, where σ_o is the far-field bending stress experienced by the beam. The bending stress is defined as $\sigma_o = 6M/BW^2$; M is the applied moment, B and W are the thickness and height of the beam, respectively. Except for the homogeneous epoxy and the bimaterial specimens for which the deviations between experiments and numerical simulations are 10%, the agreements are well within 5%. As expected, the phase angles for the cases of FGMs are small due to a dominant mode-I behavior.

6.2. Effect of crack location

The numerical simulations of the FGMs having been validated by their good agreement with the experiments, thus we proceed to perform simulations to evaluate the effect of crack location along the gradient. It would be rather intensive to obtain this information experimentally in view of the complexity of material preparation, elastic and optical characterizations. Accordingly, several finite element models were created with a mesh as shown in Fig. 6. In these, the material gradient was shifted with respect to the crack location such that cracks were located at values of $\psi = 0$, 0.08, 0.17, 0.19, 0.21, 0.25, 0.29, 0.33, 0.50, 0.58 and 1.00, respectively. For each of these 11 cases, the ratio a/W was kept at 0.3. A bimaterial having properties of $V_f = 0$ and $V_f = 0.52$, and identical loading geometry to the FGMs was also simulated. These volume fractions correspond also to those of the compliant and stiff sides of the FGM gradients, respectively. The models were symmetrically loaded with respect to the crack plane as shown in Fig. 6, so as to obtain a constant moment over a length of 60 mm.

The variation in stress intensity factor of the FGMs, normalized by that of the bimaterial counterpart, $|K_b|$, with respect to crack position along the prescribed gradient is plotted in Fig. 7(a). For a crack located on the compliant side of the gradient, the stress intensity factor of the FGM is below that of the bimaterial but rises to attain the value of the bimaterial at $\xi \sim 0.20$, and then exceeds to reach a peak at $\xi \sim 0.38$. As the crack is shifted further into the gradient, it experiences a drop in stress intensification and finally settles at a value close to that of the bimaterial. It should be noted however, that variation of $|K/K_b|$ is in a small range of 0.94–1.06. Having bench-

Table 2. Comparison of analytical and measured stress intensity factors (far-field bending stress $\sigma_o = 6M/BW^2$)

Evaluation method	$[\lvert K\rvert/\lvert\sigma_o\sqrt{(\pi a)}\rvert, \psi]$	
	CGS[a]	Plane stress FEA[b]
FGM, $\xi = 0.83$	[**1.07**, 0.4°]	[**1.06**, − 0.7°]
FGM, $\xi = 0.58$	[**1.08**, 1.0°]	[**1.11**, − 1.9°]
FGM, $\xi = 0.33$	[**1.06**, − 4.7°]	[**1.12**, − 4.3°]
FGM, $\xi = 0.17$	[**1.07**, − 2.2°]	[**1.06**, − 4.5°]
Bimaterial, $V_f = 0$ and 0.5	[**1.05**, − 0.2°]	[**1.16**, 2.5°]
Homogeneous, $V_f = 0$	[**0.98**, − 0.7°]	[**1.08**, 0.0°]
Homogeneous, $V_f = 0.5$	[**1.03**, 0.1°]	[**1.06**, 0.0°]

[a] Experimental error associated with SIF is ± 0.1 and the phase angle is ± 2.5°.
[b] Numerical error associated with SIF is ± 0.01 and ψ is ± 1° (compared with O'Dowd *et al.* [15]).

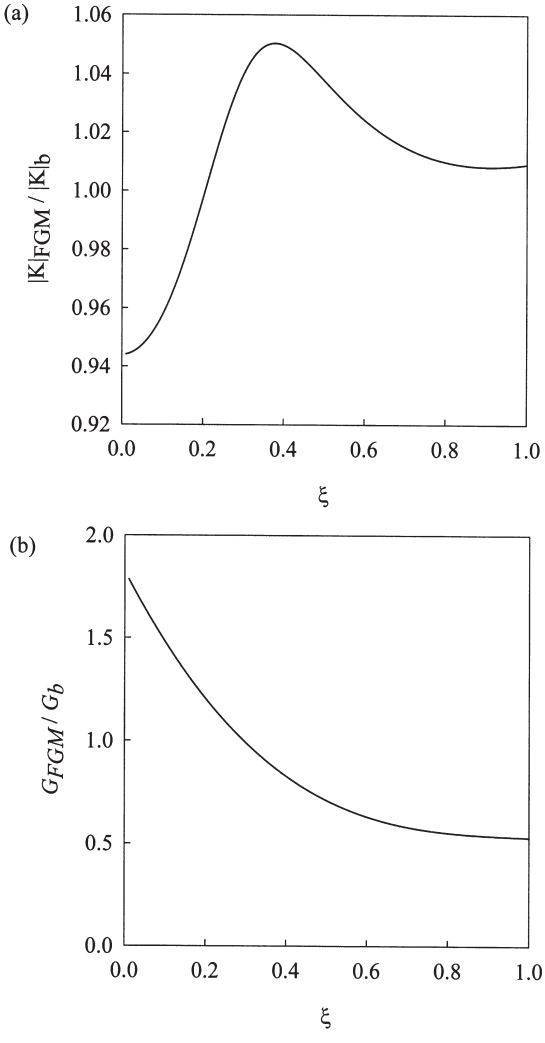

Fig. 7. Variation of (a) stress intensity factor and (b) energy release rate with ξ for FGM with $a/W = 0.3$, normalized by values for bimaterial counterparts.

marked the *K*-computation method against published results [15] to an accuracy of ± 1%, the observed variation is numerically significant.

The normalized energy release rate is obtained from the stress intensity factor by taking the local crack tip modulus into account. The ratio G_{FGM}/G_b is plotted in Fig. 7(b), and shows a monotonic decrease as the crack is moved from the compliant to the stiff side of the gradient. The energy release rate of the FGMs being initially greater than that of the bimaterial reaches that value at $\xi \sim 0.30$ and continues to decrease. These results seem to suggest that locations of crack in the range $\xi < 0.30$ are unfavorable when compared to the bimaterial counterpart. However, *it is necessary to reconcile this data with experimentally determined crack initiation values to fully assess the fracture performance*. Accordingly, in Fig. 8, the computed data is normalized by the critical crack initiation values presented in Fig. 3. Evidently, the G/G_{cr} values for the FGM are consistently lower than G/G_{bc} for the bimaterial for all crack locations ξ for the current gradient. Indeed, the fracture performance of FGMs from the standpoint of crack initiation is better by a factor of 2–3. Furthermore, the values of *G* for the FGM being normalized using the data in Fig. 3, this estimation is somewhat conservative since critical values of energy release rate under mixed-

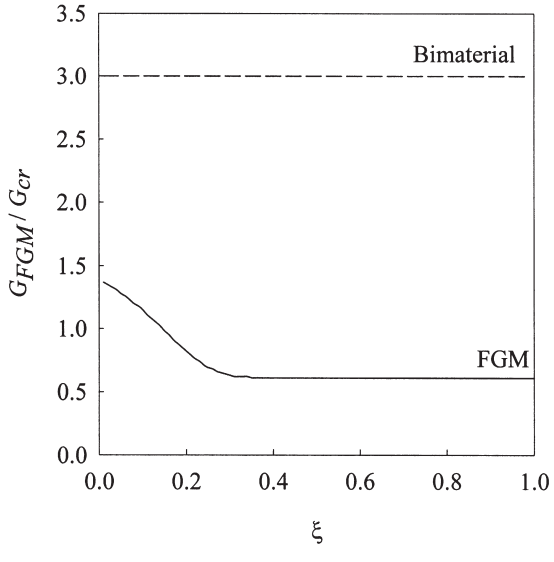

Fig. 8. Variation of energy release rate with ξ for FGM with $a/W = 0.3$ normalized by the corresponding critical values of energy release rate.

mode conditions are generally higher than pure mode-I conditions.

6.3. Effect of crack length

The influence of crack length on the fracture behavior of FGMs having cracks at varying locations along the gradient was also studied. These evaluations were performed at $\xi = 0.17$, 0.33, 0.58 and 0.83. Finite element models having the same geometry and loading configuration as shown in Fig. 6 were created for each of these crack locations, with values of $a/W = 0.1$, 0.2, 0.3, 0.4 and 0.5. In addition, bimaterial models of the same geometry were simulated and subjected to the same conditions, as a basis for comparison. The computed stress intensity factors are plotted in Fig. 9(a), normalized by $K_o = \sigma_o\sqrt{(\pi a)}$. As expected, for the same load the stress intensity factors increase with lengthening crack, following a region of constant value when crack lengths are small. This behavior is similar to the ones for homogeneous materials where the function $f(a/W)$, initially constant, increases rapidly with crack length.

Some additional interesting points must also be highlighted. First, the stress intensity factor computations suggest that the variation for the bimaterial is closer to that of a crack located in the stiff region of the FGM. Secondly, the FGM stress intensity factors increase as the cracks are relocated from the stiff side to the compliant side of the gradient. However, they suddenly drop in the vicinity of the transition region between the FGM and the compliant material. This result, shown in Fig. 7(a) for $a/W = 0.3$ seems to hold for all values of a/W. The general trend for stress intensity factor is retained when energy release rates for the FGM (G_{FGM}) are normalized by $G_o = K_o^2/E_o$, and plotted for different a/W ratios (Fig. 9(b)).

The behavior of energy release rate relative to the bimaterials, G_{FGM}/G_b, for different a/W ratios is shown in Fig. 9(c). Unlike the stress intensity factor variations (Fig. 9(a)) and normalized energy release rate with respect to a homogeneous counterpart, G_{FGM}/G_b decreases monotonically with ξ for all crack lengths. Fig. 9(d) shows the variation in FGM phase angle normalized by its bimaterial counterpart with respect to crack length. (It should be noted that phase angle for bimaterial ψ_b is non-unique and depends on the characteristic length, a, used to extract the mode-mixity.) The magnitude of phase angle decreases as the crack migrates from the compliant to the stiff side of the gradient. The effect is more pronounced with

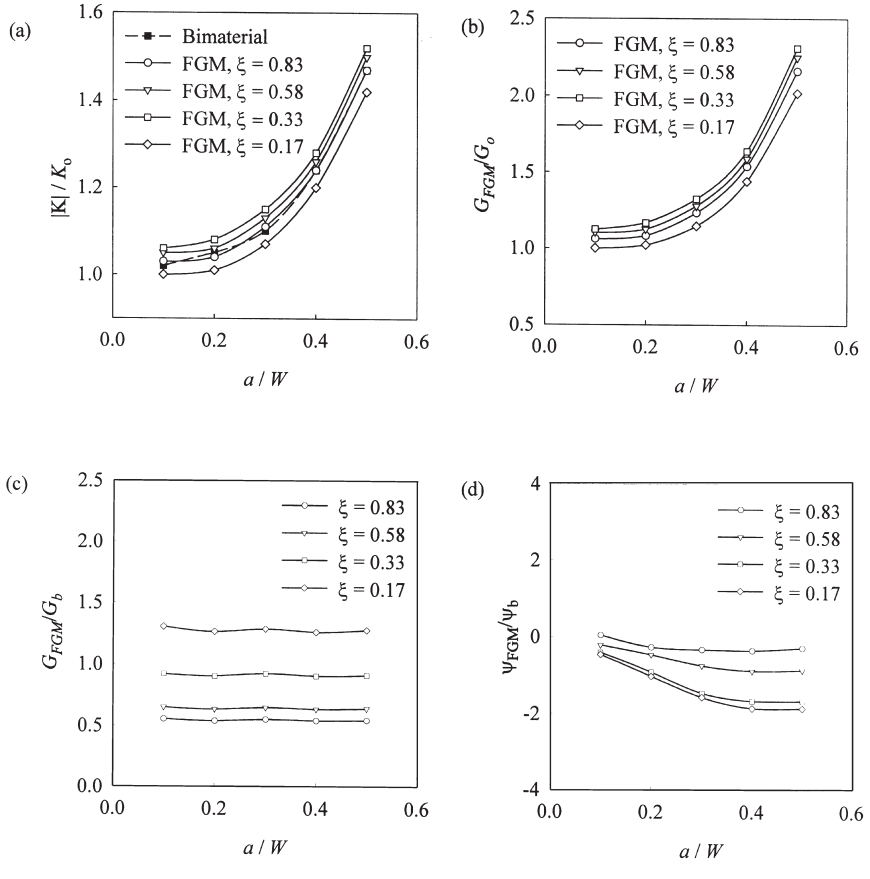

Fig. 9. Variation of fracture parameters in FGMs with crack length for different crack locations in the graded region: (a) stress intensity factor normalized by $K_o = \sigma_o\sqrt{(\pi a)}$; (b) energy release rate normalized by $G_o = K_o^2/E$; (c) energy release rate normalized by the corresponding bimaterial value, G_b; (d) phase angle normalized by the corresponding bimaterial value, ψ_b.

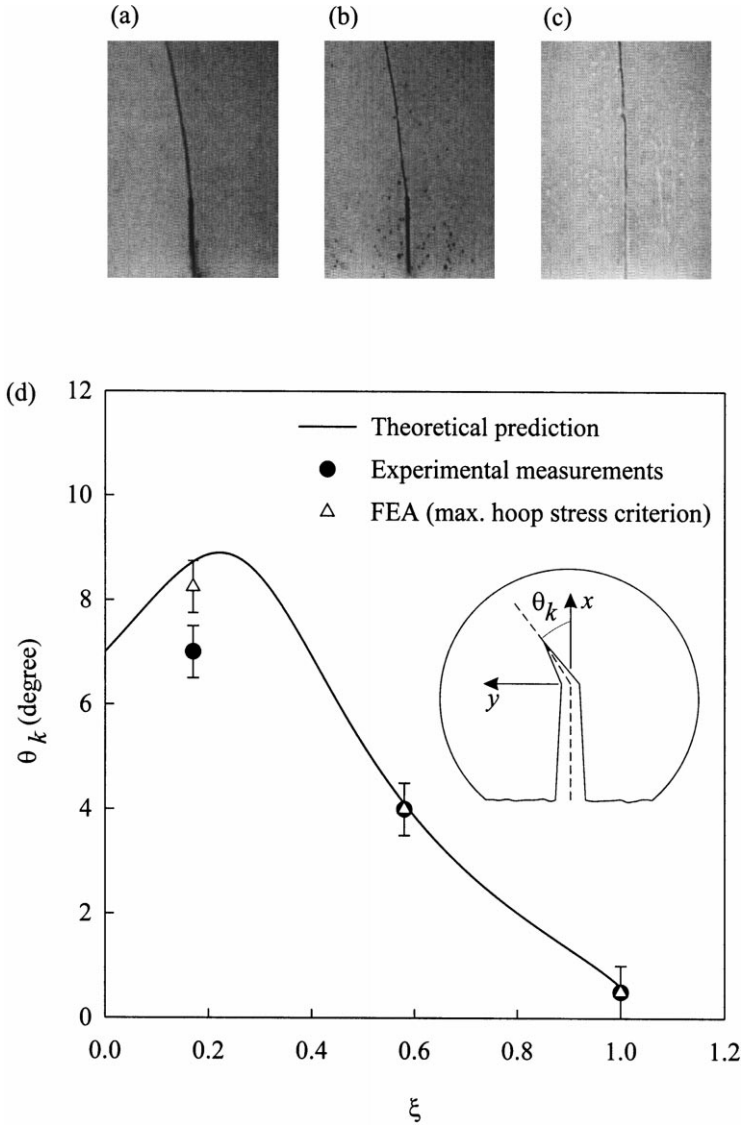

Fig. 10. Crack kinking angle in FGMs at ξ equal to (a) 0.17, (b) 0.58, and (c) 1.00; (d) variation of kink angle at all ξ locations for FGM with $a/W = 0.25$.

increasing crack length. These behavioral trends help explain deviation in crack direction when the incipient cracks are located perpendicular to the elastic gradient. Crack kinking in FGMs is discussed below.

6.4. Crack kinking

Under pure mode-I conditions, a crack will propagate in a self-similar fashion. For the cases evaluated in this study, the material possesses an inherent asymmetry relative to the crack plane, resulting in mixed-mode deformations for symmetric far-field loading. Consequently, crack tip deformations are asymmetric as evidenced by the small tilt in the CGS fringes, and the K_{II} components recorded from the analyses.

For homogeneous materials, several criteria are available to predict crack growth direction under mixed-mode conditions. These include the maximum circumferential stress criterion, the maximum energy release rate criterion, and the vanishing mode-II stress intensity factor criterion. Since crack tip behavior in FGMs depends on local homogeneity, these criteria can be applied to FGMs based on a locally homogenized model [6]. Three cases were considered for examination, with the crack at locations $\xi = 0.17$, 0.58 and 1.00 and an a/W ratio of 0.25. They were subjected to a slowly increasing moment acting symmetrically with respect to the crack plane, up to the point of failure. Fig. 10 shows the crack paths in each of these samples. The incipient cracks within each category experienced the same initial deviation to within $\pm 1°$. The measured initial propagating angles are $\theta_k = 7°$, 4° and 0.5° for $\xi = 0.17$, 0.58 and 1.00, respectively. Note also that the cracks continually change direction as they propagate. This is due to sev-

eral factors, most importantly change in specimen geometry, alteration in material asymmetry, and variation in crack tip homogeneity condition.

The angles of crack propagation criteria enumerated above are known to yield different angles of crack propagation to within one or two degrees at large values of mode mixity. The vanishing K_{II} criterion was used in this evaluation, and can be expressed as:

$$\left(\sin\frac{\theta_k}{2} + \sin\frac{3\theta_k}{2}\right)/\left(\cos\frac{\theta_k}{2} + 3\cos\frac{3\theta_k}{2}\right) = -\frac{K_{II}}{K_I} \tag{14}$$

from which predicted values of θ_k were 8.7°, 4.1° and 0.6° for $\xi = 0.17$, 0.58 and 1.00, respectively. Equation (14) was also used to predict the initial angle of propagation of cracks located at other locations ξ. The results are shown in Fig. 10. As the crack location moves further into the FGM, the kink angle increases and reaches a maximum at $\xi \sim 0.22$. The angle then decreases monotonically until the transition area between the graded and stiff homogeneous regions is reached. The angular tilt is always towards the more compliant side of the material as expected. Also shown in Fig. 10 are the angles predicted by the finite element computations based on the well-known maximum hoop stress criterion that the crack propagate normal to the local maximum tangential stress.

7. CONCLUSIONS

Mixed-mode crack tip deformations in homogeneous, bimaterial and functionally graded beams were studied. Particulate composites consisting of glass spheres dispersed within an epoxy matrix were used in this investigation. The gravity casting method was used to obtain the desired variations in Young's modulus and Poisson's ratio. Fracture tests were carried out on several specimens having different but homogeneous volume fractions to measure crack initiation parameters. The critical stress intensity factor of the glass/epoxy composite increases rapidly, but soon reaches a plateau as volume fraction is further increased. Optical measurements were conducted on FGM beams with edge cracks perpendicular to the gradient direction. Crack location was varied along the elastic gradient and the results were compared to those of bimaterial and homogeneous beams with identical geometry. Experimental fracture parameters were also compared to those from companion finite element simulations. Good agreement between experiments and computations was demonstrated. Additional finite element analyses showed that higher crack tip stress intensification and energy release rates can occur when the crack is on the compliant side of the FGM. However, when these values are reconciled with the critical values of the fracture parameters, FGMs offer better failure performance than bimaterials for all crack locations along the gradient. Variations of stress intensity factors in FGMs with respect to crack length are similar to those of homogeneous materials regardless of crack location. Fracture tests were conducted under symmetric loading to examine the effect of FGM gradient on crack kinking angle. The results compared favorably with the maximum hoop stress and vanishing K_{II} criteria based on locally homogeneous crack tip behavior. Large angles of propagation of the initial crack are observed in the compliant region, and become progressively smaller as the incipient crack is relocated toward the stiff end of the gradient.

Acknowledgements—The support of this research by NSF Materials Program (CMS-9622055) is gratefully acknowledged. The authors are also indebted to Mr Michael J. Maleski for preparing the specimens used in this study.

REFERENCES

1. Abboud, J. H., West, D. R. F. and Rawlings, R. D., *J. Mater. Sci.*, 1994, **29**, 3393.
2. Jung, J. and Kanninen, M. F., *ASME PVP Conf.*, 1982, **58**, 91.
3. Marple, B. R. and Boulanger, J., *J. Am. Ceram. Soc.*, 1994, **77**(10), 2747
4. Bao, G. and Cai, H., *Acta mater.*, 1996, **45**(3), 1055
5. Gu, P. and Asaro, R. J., *Int. J. Solids Struct.*, 1997, **34**(1), 1
6. Gu, P. and Asaro, R. J., *Int. J. Solids Struct.*, 1997, **34**(24), 3085
7. Erdogan, F., Kaya, A. C. and Joseph, P. F., *ASME J. Appl. Mech.*, 1991, **58**, 410.
8. Jin, Z. -H. and Noda, N., *ASME J. Appl. Mech.*, 1994, **61**, 738.
9. Tohgo, K., Sakaguchi, M. and Ishii, H., *JSME Int. J. — I*, 1996, **39**(4), 479
10. Sekine, H. and Afsar, A. M., *JSME Int. J. — A*, 1999, **42**(4), 592
11. Marur, P. R. and Tippur, H. V., *Int. J. Solids Struct.*, 2000, **37(38)**, 5353.
12. Butcher, R. J., Rousseau, C.-E. and Tippur, H. V., *Acta mater.*, 1999, **47**(1), 259
13. Weng, G. J., *Int. J. Engng Sci.*, 1984, **22**(7), 845
14. Moloney, A. C., Kausch, H. H., Kaiser, T. and Beer, H. R., *J. Mater. Sci.*, 1987, **22**(2), 381
15. O'Dowd, N. P., Shih, C. F. and Stout, M. G., *Int. J. Solids Struct.*, 1992, **29**(5), 571
16. Xu, L. and Tippur, H. V., *Int. J. Fract.*, 1995, **71**, 345.
17. Liechti, K. M. and Chai, Y. S., *ASME J. Appl. Mech.*, 1991, **58**, 680.
18. Tippur, H. V., Krishnaswamy, S. and Rosakis, A. J., *Int. J. Fract.*, 1991, **48**, 193.
19. Rice, J. R., *ASME J. Appl. Mech.*, 1988, **55**, 98.
20. Rosakis, A. J. and Ravi-Chandar, K., *Int. J. Solids Struct.*, 1986, **22**, 121.
21. Sinha, J. K., Tippur, H. V. and Xu, L., *Int. J. Solids Struct.*, 1997, **34**(6), 741
22. Lee, Y. -D. and Erdogan, F., *Int. J. Fract.*, 1995, **69**, 145.
23. Giannakopoulos, A. E. and Suresh, S., *Int. J. Solids Struct.*, 1997, **34**(19), 2357